High-speed spiral imaging technique for an atomic force microscope using a linear quadratic Gaussian controller

H. Habibullah, H. R. Pota, and I. R. Petersen

Citation: Review of Scientific Instruments **85**, 033706 (2014); doi: 10.1063/1.4868249
View online: http://dx.doi.org/10.1063/1.4868249
View Table of Contents: http://aip.scitation.org/toc/rsi/85/3
Published by the American Institute of Physics

High-speed spiral imaging technique for an atomic force microscope using a linear quadratic Gaussian controller

H. Habibullah,[a] H. R. Pota,[b] and I. R. Petersen[c]
School of Engineering and Information Technology, University of New South Wales, Canberra, Australian Capital Territory 2612, Australia

(Received 1 December 2013; accepted 27 February 2014; published online 20 March 2014)

This paper demonstrates a high-speed spiral imaging technique for an atomic force microscope (AFM). As an alternative to traditional raster scanning, an approach of gradient pulsing using a spiral line is implemented and spirals are generated by applying single-frequency cosine and sine waves of slowly varying amplitudes to the X and Y-axes of the AFM's piezoelectric tube scanner (PTS). Due to these single-frequency sinusoidal input signals, the scanning process can be faster than that of conventional raster scanning. A linear quadratic Gaussian controller is designed to track the reference sinusoid and a vibration compensator is combined to damp the resonant mode of the PTS. An internal model of the reference sinusoidal signal is included in the plant model and an integrator for the system error is introduced in the proposed control scheme. As a result, the phase error between the input and output sinusoids from the X and Y-PTSs is reduced. The spirals produced have particularly narrow-band frequency measures which change slowly over time, thereby making it possible for the scanner to achieve improved tracking and continuous high-speed scanning rather than being restricted to the back and forth motion of raster scanning. As part of the post-processing of the experimental data, a fifth-order Butterworth filter is used to filter noises in the signals emanating from the position sensors and a Gaussian image filter is used to filter the images. A comparison of images scanned using the proposed controller (spiral) and the AFM PI controller (raster) shows improvement in the scanning rate using the proposed method. © *2014 AIP Publishing LLC*. [http://dx.doi.org/10.1063/1.4868249]

I. INTRODUCTION

Multi-disciplinary uses of the atomic force microscope (AFM) have made it an attractive tool in the fields of atomic resolution surface measurements, nano-robotics, nano-manipulation, nano-fabrication, nano-lithography, and nano-range material handling such as pushing, pulling, cutting, rolling, and sliding.[1–5] A piezoelectric tube actuator (PTA) plays a vital role in precision motion generation for applications of the AFM and other scanning probe microscopes (SPMs). The use of this actuator was introduced during World War I in sonar and after World War II, in sonar, acoustic, and accelerometer studies[6] which provide a good starting point for using piezoelectric materials as actuators, sensors, motors, damage detectors, active and passive vibration control devices, and structural dampers as well as for nanopositioning, nanomanipulation, etc. The invention of the scanning tunnelling microscope (STM), scanning probe microscopes such as the AFM, scanning electron microscope (SEM), and transmission electron microscope (TEM) have revolutionized research in various areas, e.g., materials science, nano-biotechnology, nano-medicine, nano-pharmaceutics, precision mechanics, optics, microelectronics, etc.[7,8] The STM has a limitation that it can scan only conductive samples or those coated with conductive layers and this has been overcome through the invention of the AFM.[8] In recent years, the AFM has been widely used to generate three dimensional (3D) images of material surfaces, and biological specimens with ultra-high accuracy.[9]

AFM-based image scanning is achieved by applying a small, gradually increasing gradient staircase or ramp signal in the y direction while concurrently applying a triangular signal along the x direction. One of the main drawbacks of this scanning method is that its spatial resolution is poor as the triangular signal contains all of the odd harmonics of the fundamental frequency. In raster scanning, the scanning speed is usually limited to 1%–10% of the first resonant frequency of the piezoelectric tube (PZT) scanner.[9] When a triangular signal is applied to the PZT, one of the high-frequency harmonics excites the resonance and a distorted triangular output is produced at the free end of the PZT along the X-axis which generates a distorted image. In the SPM and other scanner devices, such as selective laser sintering machines (SLSs), tracking the triangular signal is a major challenge.[10]

Feedback control techniques to improve the accuracy and speed of the AFM have been reported in the literature.[11–17] A signal transformation method is implemented to track the reference triangular signal in an AFM in Ref. 18. A H^∞ controller[19] achieves a scanning rate of 125 Hz, as reported.[19] Creep, hysteresis, and vibration effects are minimized by implementing a proportional plus derivative high-gain feedback controller and feed-forward controller.[15] PZT materials have resonant natures due to their mechanical properties which are also responsible for distorting the output triangular signal and scanned images. Damping the resonant peak of the PZT is a second major issue in the accurate positioning of the AFM's scanner. A survey of damping controllers is given in Ref. 20.

[a]Electronic mail: h.habib@student.adfa.edu.au
[b]Electronic mail: h.pota@adfa.edu.au
[c]Electronic mail: i.petersen@adfa.edu.au

The integral resonant controller is another approach for attenuating the vibration due to the resonant mode of the PZT.[21] Despite significant performance improvements of the PZT scanner, it remains difficult to track fast triangular signals due to the non-linearities and low bandwidth of the scanner tube.

The raster scanning produces images with deformed surface topography, which leads to misinterpretations of the original data while drifting occurs which may cause the image to be oblique; for example, a square lattice becomes rhombohedral and since this is a well-known structure, one can draw the wrong conclusions. To avoid this, spiral scanning approaches have been introduced in Refs. 22–27 for fast imaging using the AFM. Perhaps the idea of spiral scanning was first introduced in medical imaging in 1976.[28] In Ref. 29, a spiral scanning method is reported as a replacement for raster scanning and in this scanning two challenges are mentioned. The first challenge is the uniform distribution of sampling points in 2D plane and the second is relatively constant linear speed. A detail image construction procedure is also described in Ref. 29 but the images are worse than the images scanned using the proposed scheme. A specially designed AFM head is used for spiral scanning[30] where the AFM head is mounted on a spindle for generating rotational motion and a turning machine is used to turn a sample, but it is hard to maintain the relative position of the head and sample. A fast spiral scanning technique is also reported in Ref. 31, for medical magnetic resonance imaging (MRI). A cycloid scanning approach is described in Ref. 32. Actually, cycloid scan takes longer time than the spiral scan, to cover a definite area on a sample at the same scanning frequency. The reason is that, during cycloid scan there is an extra ramp signal to flow the scan throughout the X-axis and at the same time it involves overlapping of the data points.[32] On the other hand, spiral scan involves simultaneous application of sine and cosine signals in both the X and Y-PTSs, which results in continuously increasing circles with no overlapping among the data points traced on the sample surface.

An approach of gradient pulsing using a spiral line is implemented in this paper. The entire area is uniformly covered by a form of spiral scanning whereby a circular symmetrical area for fast AFM imaging, which is different from that determined from raster scanning, is obtained. Externally generated cosine and sine waves of slowly varying amplitudes are applied to the PZT scanners X and Y-axes to force it to move along spiral lines with varying instantaneous radii. The resultant spiral signal has a low-frequency content which moves slowly over time and regulates the tracking performance through continuous high-frequency imaging. These generated spirals, called Archimedean spirals[33] are shown in Fig. 1. The distance between two consecutive lines is known as the pitch (p) which has the property of being constant over the sample surface and makes it possible to uniformly scan a surface without missing any information.[34] As both axes are forced by single-frequency sinusoidal signals, the resulting system is in the steady state and avoids the transient behavior that can be observed in raster scanning in which the probe moves from one line to the next. With only some software modifications, the proposed scanning method can be used for faster scanning in a commercial AFM.

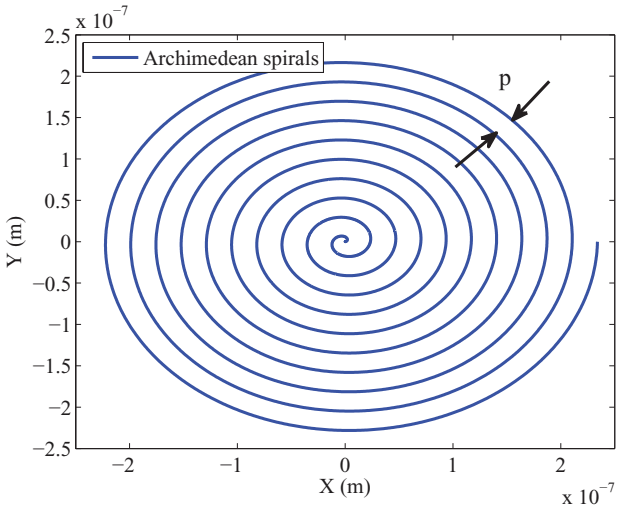

FIG. 1. Spiral lines.

The remainder of this paper is organized as follows: Sec. II presents the spiral generation procedure; Sec. III explains the modeling of the PTS scanner; Sec. IV discusses the controller design procedure for tracking the reference sinusoids and damping the resonant mode of the PTS; Sec. V presents the performance of the controller, improvement of the scanning speed, and quality of images; and Sec. VI provides conclusions.

II. BASIC MATHEMATICS FOR SPIRAL GENERATION

The most popular 3D Fourier imaging algorithm with three time varying gradient fields is

$$G(t) = \iiint \sigma(x, y, z) \exp\left[i\gamma \int_0^t x G_x(t) + y G_y(t) dt\right] \exp\left(\frac{t}{T_2}\right) dx dy dz, \quad (1)$$

where, $G(t)$ is the free induction decay (FID) signal, which is a time domain signal, that remains unaffected by any gradient and decays exponentially, $\sigma(x, y, z)$ is the spin density distribution, and $G_x(t)$, $G_y(t)$, and $G_z(t)$ are the time-varying gradient fields of the x, y, and z coordinates, respectively. The exponential term $\exp(t/T_2)$ is the T_2 decay term that often appears as a limiting factor in high-resolution imaging. The time constant that determines the rate of decay is known as T2-decay. In real time application this decay rate is unpredictable.[34,35] Original T2 decay is a function of completely random interactions between spins.

The general 3D imaging equation can be converted to 2D forms for analysis and the T_2 decay term can be ignored for simplicity.[34] The FID signal obtained for a 2D plane at $z = z_0$ is

$$G(t) = \iint \sigma(x, y, z_0) \exp\left[i \int_0^t x V_x(t) + y V_y(t)\right] dx dy; \simeq G((V_x, V_y), \quad (2)$$

where, $V_x = \gamma \int_0^t G_x(t) dt$

and

$$V_y = \gamma \int_0^t G_y(t)dt. \tag{3}$$

From (2) and (3) it can be shown that, $\sigma(x, y)$ and $G((V_x, V_y)$ are a Fourier transform pair.

The slowly varying amplitudes of the sinusoidal pulse pair will result in a set of circularly symmetrical concentric circles with different instantaneous radii as

$$\begin{aligned} V_x(t) &= \gamma \eta_i(t) \cos \omega t, \\ V_y(t) &= \gamma \eta_i(t) \sin \omega t, \end{aligned} \tag{4}$$

where, $\eta_i(t)$ is the discrete amplitude at time t and ω is frequency of the sine wave.

Continuous rather than discrete circles, i.e., complete spiral motions can be obtained from simple modification of (4), which would be easier to implement in a physical system as

$$\begin{aligned} V_x(t) &= R \cos \omega t, \\ V_y(t) &= R \sin \omega t, \end{aligned} \tag{5}$$

where, $R = \gamma \eta t$ is the instantaneous radius of the spiral at time t. The area of a sample to be scanned in a spiral trajectory of pitch p at a linear velocity v and if the instantaneous radius R with angular velocity ω (rad/s) at any time t,

$$\omega = \frac{v}{R} \tag{6}$$

and

$$\frac{dR}{dt} = \frac{p\omega}{2\pi}. \tag{7}$$

Integrating (2) we have

$$R = \frac{p\omega t}{2\pi}, \tag{8}$$

where R = 0 at t = 0 and pitch p calculated as

$$p = \frac{2R}{\text{number of spiral curves} - 1}, \tag{9}$$

where number of spiral curves is the number of crossing points on $y = 0$ or $x = 0$ line. The spirals generated with defined parameter is applied to move the PTS of the AFM in spiral scanning. Simultaneous application of these two signals in (5) results in continuously increasing circles, which create complete spiral positioning on a sample surface, as shown in Fig. 2.

III. MODELING OF THE PTS

In the design of the proposed control scheme, the PTS is modeled as a single-input single-output (SISO) system. An experimental frequency response is obtained using a dual-channel HP35665A dynamic signal analyser (SA). In this work, our experimental setup consists of the NT-MDT Ntegra scanning probe microscope (SPM) that is configured as an AFM. The experimental setup contains some other parts such as signal access module (SAM), control electronics, vibration isolator, and a computer to operate the NOVA software. Other accessories are a DSP dSPACE board and high-voltage amplifier (HVA) with a constant gain of 15 which supplies power to

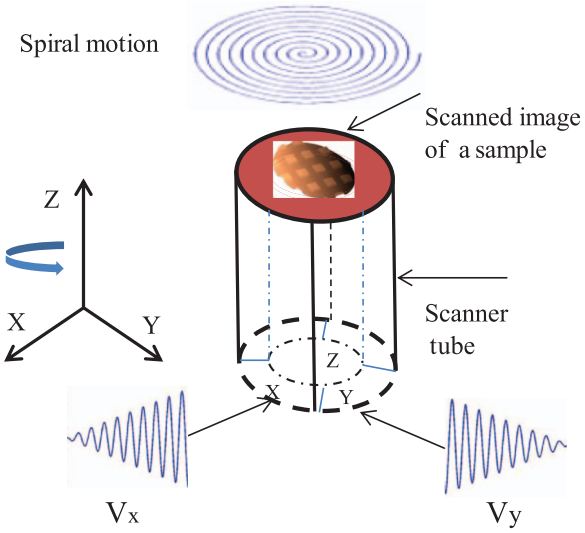

FIG. 2. A schematic view of the PTS.

the X, Y, and Z-PTSs using the SAM as an intermediate device. The scanner is a NT-MDT z50313cl PI type which scans by sample in the constant force mode. The (X, Y, Z) scanning range is 100 μm × 100 μm × 12 μm and resonant frequency for both X and Y is 900 Hz, and 5 kHz for Z-PTS, that performs X, Y, and Z positioning in the AFM. Displacements of the X, Y, and Z-PTSs are obtained from capacitive position sensors incorporated with the AFM. The experimental connection is shown in Fig. 3. The frequency responses generated in the SA are processed in MATLAB and using the prediction error method (PEM), a system model is obtained.[36,37] The best-fit model frequency responses for the X and Y-PTSs are shown in Fig. 4.

The following state-space model is found to be the best fit for the X-PTS, as illustrated in Fig. 4(a), the resonant mode of which is at about 834.5 Hz:

$$\dot{x_x} = a_x x_x + b_x u_x, \tag{10}$$

$$y_x = c_x x_x + d_x u_x, \tag{11}$$

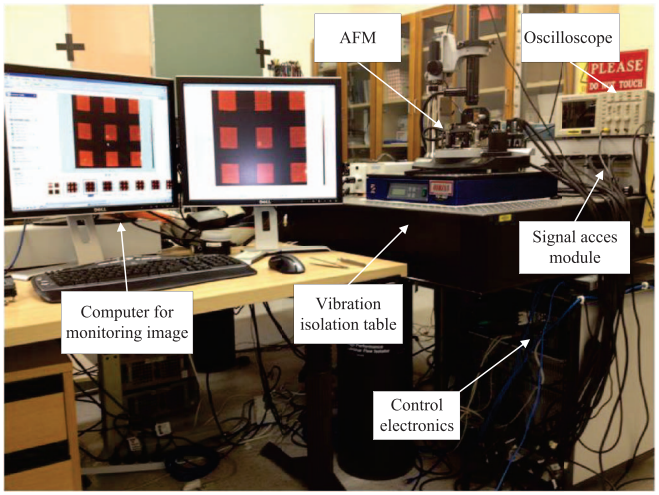

FIG. 3. Experimental setup used in the AFM positioning.

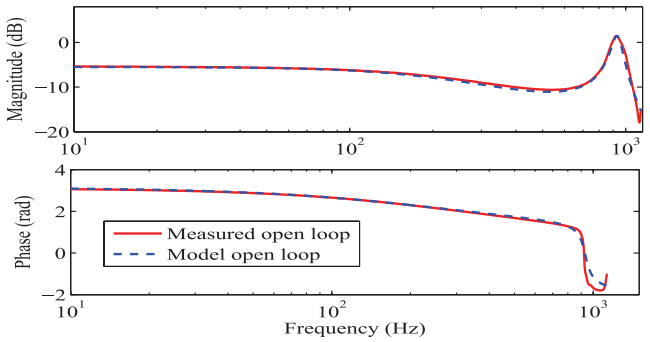

(a)

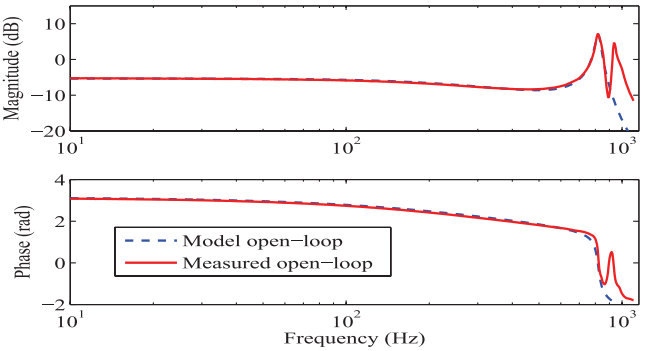

(b)

FIG. 4. Frequency response plots of measured and identified system models for (a) input to the X-PTS and output from the X position sensor, (b) input to the Y-PTS and output from the Y position sensor.

$$a_x = \begin{bmatrix} -291.1 & -6143.5 & 3600 \\ 3564.8 & -755.4 & 4195 \\ -275.8 & -2578.7 & -639.3 \end{bmatrix}; \quad b_x = \begin{bmatrix} -4.5424 \\ 10 \\ 10 \end{bmatrix};$$

$$c_x = \begin{bmatrix} 37.4411 & 47.1767 & -59.3637 \end{bmatrix}; \quad d_x = \begin{bmatrix} 0 \end{bmatrix},$$

where, x_x is the state of the X-PTS, y_x is the output of the X-PTS, a_x is the system matrix, b_x is input to the plant, c_x and d_x are the output matrices from the plant. Similarly, the following state-space model is found to be the best fit for the Y-PTS, as illustrated in Fig. 4(b) where the resonant mode of the PTS is at about 815.2 Hz:

$$\dot{x_y} = a_y x_y + b_y u_y, \tag{12}$$

$$y_y = c_y x_y + d_y u_y, \tag{13}$$

$$a_y = \begin{bmatrix} 14.1 & -6376.5 & 3405.9 \\ 3625.7 & -654.9 & 3080 \\ 28.3 & -1058.9 & -1058.7 \end{bmatrix}; \quad b_y = \begin{bmatrix} -3.0969 \\ 12.5441 \\ 9.8753 \end{bmatrix};$$

$$c_y = \begin{bmatrix} 35.1709 & 46.7633 & -62.4762 \end{bmatrix}; \quad d_y = \begin{bmatrix} 0 \end{bmatrix},$$

where, x_y is the state of the Y-PTS, y_y is the output of the Y-PTS, a_y is the system matrix, b_y is the input matrix to the plant, c_y and d_y are the output matrices from the plant. In Fig. 4, we can see that both of these PTS plants have a 180° phase shift at low frequencies and zeros in the right half plane. In the modeling of the PTSs, only the first resonant modes are considered.

IV. CONTROLLER DESIGN

A. Design of LQG controller for reference tracking

A linear quadratic Gaussian (LQG) controller is designed for minimizing the steady-state error and tracking the reference sinusoidal signal. An internal reference model-based optimal LQG controller is designed for both the X and Y-axes of the PTS's, with the following two identified SISO state-space plant models considered for the X and Y-PTSs:

$$\dot{x} = ax + bu, \tag{14}$$

$$y = cx + du, \tag{15}$$

where a, b, c, and d are the state-space matrices of the model plant (X-PTS/Y-PTS), as stated in (10) and (12), u is the input, y is the measured output, and x is the state vector with a dimension of 3. We write the state vector (x) as

$$x = \begin{bmatrix} x_1 \\ x_2 \\ x_3 \end{bmatrix}.$$

One of the objectives of the control design is to control the system error by incorporating it in the controller as a replacement for one of the states x_1, of the plant.[38] The system error is defined as the difference between the reference input and plant output as

$$e' = y_r - y, \tag{16}$$

where y_r is the sinusoidal reference input to the plant and assumed to satisfy the differential equation:

$$\dot{\hat{y}_r} = A_r \hat{y}_r, \tag{17}$$

$$A_r = \begin{bmatrix} 0 & -\omega^2 \\ 1 & 0 \end{bmatrix},$$

$$\hat{y}_r = \begin{bmatrix} y_{r_1} \\ y_{r_2} \end{bmatrix},$$

where A_r is the state matrix for the reference signal and ω is the frequency of the input signal. In this design the sinusoidal reference input is modeled and the error dynamic equation is

$$\dot{e'} = \dot{y_r} - \dot{y}. \tag{18}$$

To account for the steady-state error, integral action is considered for the error state (e'), i.e.,

$$e'_I = \int e' dt. \tag{19}$$

Now, the error dynamics, i.e., the converted state-space model is

$$\dot{x_e} = Ax_e + Bu_e + Ey_r, \tag{20}$$

$$y_e = Cx_e, \tag{21}$$

where A, B, and C are the state-space matrices of the modified plant, E is the exogenous input matrix, u_e is the input to the modified plant, y_e is the measured output from that plant, and x_e is the state vector with dimensions of 4×1, where the state vector of the modified error dynamics model (x_e) is

$$x_e = \begin{bmatrix} e_I' \\ e' \\ x_2 \\ x_3 \end{bmatrix}.$$

Therefore, the entire state of (17) and (20) satisfies the following differential equation:[38]

$$\dot{x}_m = A_m x_m + B_m u_m, \tag{22}$$

$$y_m = C_m x_m, \tag{23}$$

$$A_m = \left[\begin{array}{c|c} A & E \\ \hline 0 & A_r \end{array}\right],$$

$$B_m = \begin{bmatrix} B \\ \hline 0 \end{bmatrix},$$

$$C_m = \left[\begin{array}{c|c} C & 0 \end{array}\right],$$

where A_m, B_m, and C_m are the state-space matrices of the meta-system, u_m is the input of the meta-system, y_m is the measured output from that plant, and x_m is the meta-state vector. This x_e is the sub-state of the x_m.

Since the exogenous states are generally not controllable, the appropriate performance integral is

$$J = \int_0^\infty [x_e{}' Q x_e + u_e{}' R u_e] dt, \tag{24}$$

where Q is the state weighting matrix and R is the control weighting, which is scalar. The weighting matrix for the meta system (22) is

$$Q_m = \left[\begin{array}{c|c} Q & 0 \\ \hline 0 & 0 \end{array}\right].$$

The performance matrix for the meta-system in (22) is[38]

$$\hat{M} = \left[\begin{array}{c|c} \hat{M}_1 & \hat{M}_2 \\ \hline \hat{M}_2{}' & \hat{M}_3 \end{array}\right],$$

where $\hat{M}$ is the performance matrix for the meta-system, $\hat{M}_1$, $\hat{M}_2$, $\hat{M}_2{}'$, and $\hat{M}_3$ are the performance matrices corresponding to the subsystems of the meta-system (22). Now the gain for the meta-system is

$$\hat{G_m} = \left[\begin{array}{c|c} R^{-1} B' \hat{M}_1 & R^{-1} B' \hat{M}_2 \end{array}\right],$$

where G_m is composed of the gains $G_e = R^{-1} B' \hat{M}_1$ and $G_r = R^{-1} B' \hat{M}_2$. G_e is a state feedback gain for the modified plant and G_r is the feed-forward gain for the reference input signal which acts against exogenous effects, i.e., the effects of the reference signal and external disturbance.

The minimizing matrix ($\hat{M}$) resulting from the minimizing gain ($\hat{G_m}$) must satisfy the following differential equation:

$$-\dot{\hat{M}} = \hat{M} A_m + A_m{}' \hat{M} - \hat{M} B_m R^{-1} B_m{}' \hat{M} + Q_m. \tag{25}$$

The solution to this equation will give the gain matrix ($\hat{G_m}$) and by putting the value of $\hat{M}$ in (25) and performing matrix multiplication, the differential equations for the sub-matrices are obtained as

$$\begin{aligned} -\dot{\hat{M}}_1 &= \hat{M}_1 A + A' \hat{M}_1 - \hat{M}_1 B R^{-1} B' \hat{M}_1 + Q; \\ -\dot{\hat{M}}_2 &= \hat{M}_1 E + \hat{M}_2 A_r + A_c{}' \hat{M}_2; \\ A_c &= A - B R^{-1} B' \hat{M}_1, \end{aligned} \tag{26}$$

where A_c is the closed-loop dynamics matrix of the regulator subsystem. It is seen from the formula for $\hat{G_m}$ that the sub-matrix ($\hat{M}_3$) of the performance matrix ($\hat{M}$) is not required to find the gain for the meta-system.[38]

The steady-state solution for $\hat{M}_2$ can be found and must satisfy:

$$0 = \hat{M}_1 E + \hat{M}_2 A_r + A_c{}' \hat{M}_2, \tag{27}$$

where $\hat{M}_1$ is the solution to the algebraic Riccati equation of the regulatory sub-system and $\hat{M}_2$ can be found from the above equation. Thus, we have the necessary gains to realize the control law in Ref. 38,

$$u_m = -R^{-1} B' \hat{M}_1 x_e - R^{-1} B' \hat{M}_2 y_r. \tag{28}$$

A block diagram of the control implementation is shown in Fig. 5.

The calculated gains for the optimal LQG controller augmented with the vibration compensator for the X-PTS are $K_{Ix} = 55.8$, $K_{ex} = 0.0714$, $K_{x2} = 0.1604$, $K_{x3} = -0.6658$, $K_{x4} = 0.2304$, $K_{x5} = -0.9158$, and the feed-forward gain $G_{rx} = 1.88$ and for the Y-PTS, $K_{Iy} = 130$, $K_{ey} = 0.4753$, $K_{y2} = 12.3199$, $K_{y3} = 0.7257$, $K_{y4} = 5.2199$, $K_{y5} = 0.0753$, and feed-forward gain $G_{ry} = 1.67$. Where K_I the gain for integral state, K_e the gain for the error state e', K_{x2} the gain for x_2 state, K_{x3} the gain for the x_3 state, K_{x4} the gain for the x_4 state, K_{x5} the gain for the x_5 state, and G_r for feed-forward gain. The suffix x for the X-PTS and y for the Y-PTS.

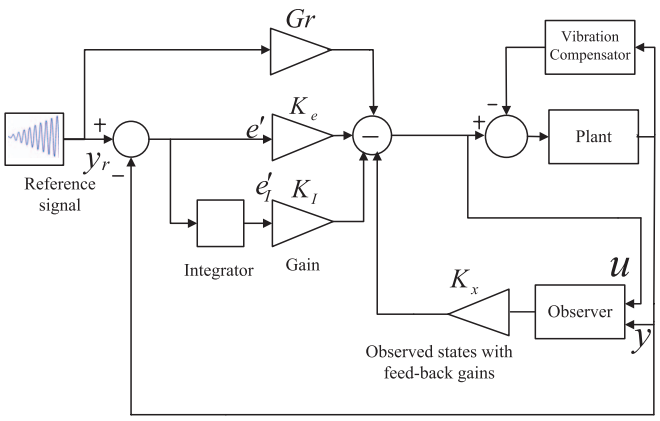

FIG. 5. Block diagram for implementation of the proposed controller.

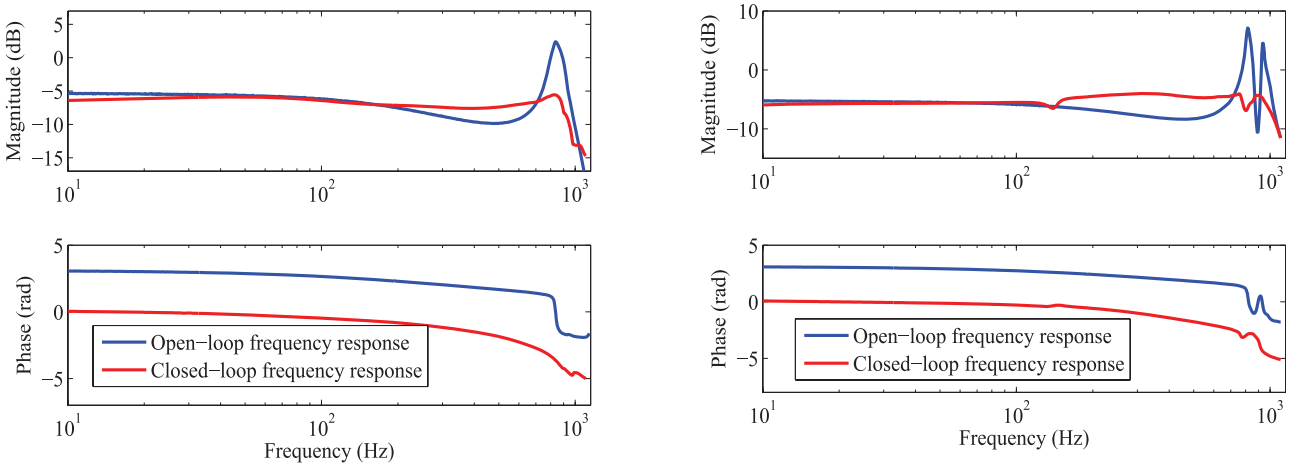

FIG. 6. A comparison of the frequency responses using an optimal LQG controller with a vibration compensator and open-loop (a) X-PTS and (b) Y-PTS.

B. Design of the Kalman observer

A Kalman observer can be used as a state-observer and noise filter[39] and displacements of the PTSs are obtained from the sub-nanometric resolution position sensors.[40] However, the sensors add unwanted noise and disturbances to the output displacement signal, to remove which we design a Kalman state observer as a noise filter. A sensor measures the output from a PTS plant not its states as, in a regulatory system, all its states should be known, and the Kalman state observer estimates them from the measured output.[38] The Kalman observer dynamics are as follows:

$$\dot{\hat{x}} = (a - Lc)\hat{x} + bu + Ly, \tag{29}$$

$$\hat{y} = \hat{c}\hat{x}, \tag{30}$$

where $\hat{x}$ is the estimated state, $\hat{y}$ is the estimated output, $\hat{c}$ is an identity matrix of dimensions $n \times n$, and L is the observer gain which depends on the Gaussian white noise, process noise covariance, and measurement noise covariance. A block diagram of the control implementation is shown in Fig. 5.

C. Design of a vibration compensator

In this section, we discuss the design of a vibration compensator for damping the resonant mode of the PTS. Although the LQG controller has some damping capacity, a vibration compensator is introduced to achieve better damping and higher bandwidth. From the experimental frequency responses of the PTSs, we know that the first resonance occurs at 834.5 Hz for the X-PTS and 815.2 Hz for the Y-PTS. This compensator is designed to damp the first resonant mode of each of the PTSs with a bandwidth close to its first resonant frequency. The general form of the resonant compensator $K_i(s)$ is given in Refs. 41 and 42:

$$K_i(s) = \sum_{i=1}^{n} -k_{ci} \frac{(s^2 + 2\zeta_i \omega_i s)}{s^2 + 2\zeta_i \omega_i s + {\omega_i}^2}, \tag{31}$$

where ω_i is the ith controller's center frequency which is the frequency at the ith resonant peak of the plant, $k_{ci}(s)$ is the controller gain, and ζ is the damping factor of the corresponding mode. In fact, the controller $K_i(s)$ is a second-order band-pass filter and has a high gain at the resonant frequency of the plant which is a means of suppressing the vibration so that the gain suddenly drops away from the resonant frequency. Of the controller parameters, i.e., ω and ζ, ω has a greater effect on damping of the resonant mode than the damping factor ζ. If we vary ζ by $\pm 10\%$, there will be a noticeable effect on damping. But if we vary ω by $\pm 5\%$, the attenuation performance will be significantly decreased and, once the value of ω is fixed, the parameter k_{ci} plays an important role in damping.

V. THE PERFORMANCE OF THE CONTROLLER

A. Frequency domain performance

A frequency-domain performance evaluation of the proposed controller is conducted to compare the measured open-loop and closed-loop frequency responses for the X and Y-PTSs, as shown in Fig. 6. It demonstrates that there is significant damping of the resonant mode of each PTS (10 dB for the X-PTS and 16 dB for the Y-PTS) and a higher closed-loop bandwidth close to its first resonant frequency has been achieved.

B. Tracking performance

The tracking performance of the proposed scheme is presented in Fig. 7 at frequencies 10, 30, 60, and 120 Hz. These results demonstrate that the proposed control approach achieves improved tracking of the reference signal and improved spiral positioning of the scanner tube. Spiral tracking at 10, 30, and 60 Hz frequencies are quite good as shown in Figs. 7(c), 7(f), and 7(i). At 120 Hz a significant distortion (elliptical shape) is observed as shown in Fig. 7(l). A fifth-order Butterworth filter is used to filter the measured (dotted line) noisy signal and, as can be seen in Fig. 7, the filtered (solid

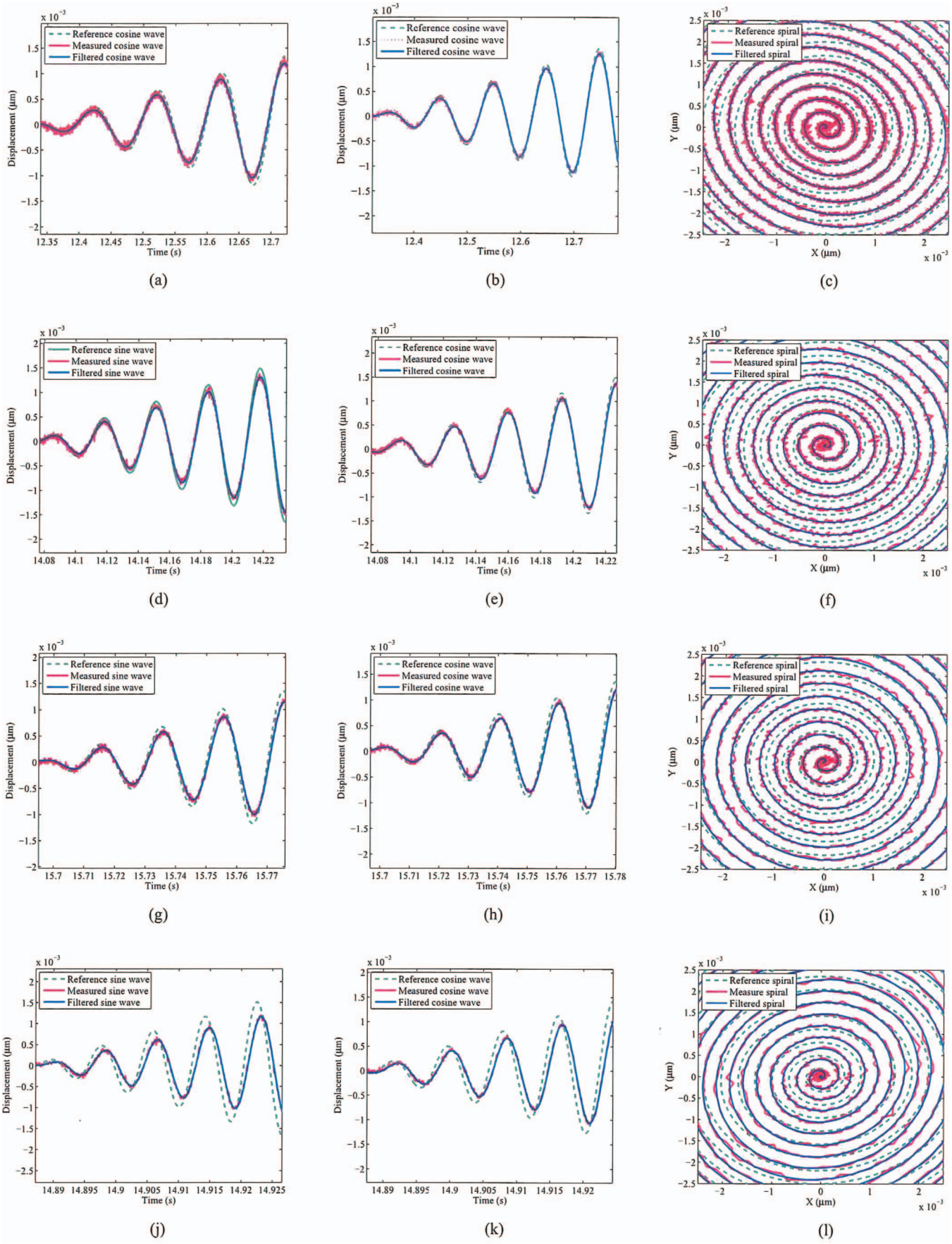

FIG. 7. Tracking performance of the proposed controller at different frequencies. (a) 10 Hz sine, (b) 10 Hz cosine, (c) 10 Hz spiral, (d) 30 Hz sine, (e) 30 Hz cosine, (f) 30 Hz spiral, (g) 60 Hz sine, (h) 60 Hz cosine, (i) 60 Hz spiral, (j) 120 Hz sine, (k) 120 Hz cosine, and (l) 120 Hz spiral.

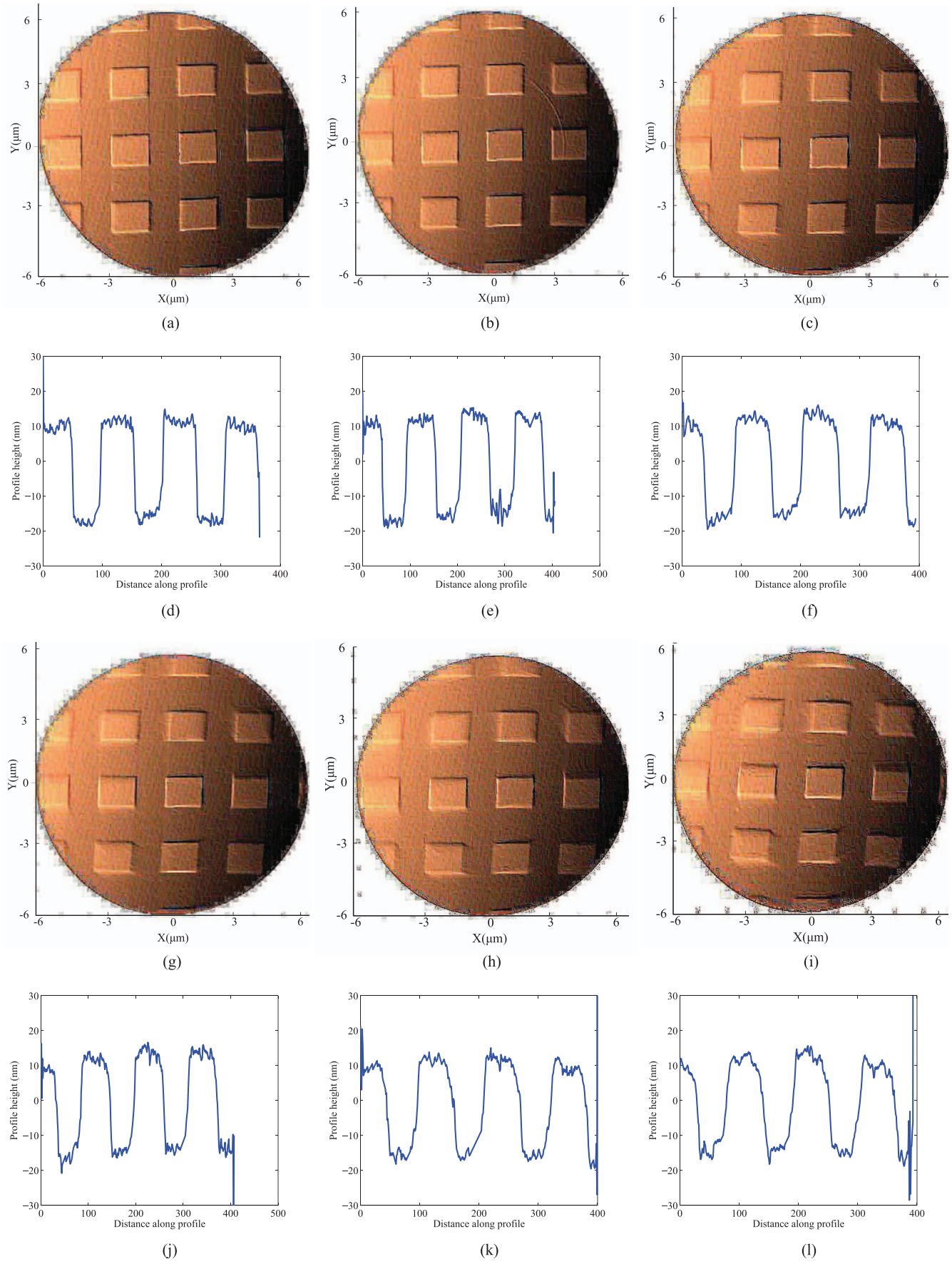

FIG. 8. Spiral scanned images along with their intensity profiles. (a) 10 Hz, (b) 30 Hz, (c) 60 Hz, (d) 10 Hz, (e) 30 Hz, (f) 60 Hz, (g) 120 Hz, (h) 150 Hz, (i) 180 Hz, (j) 120 Hz, (k) 150 Hz, and (l) 180 Hz.

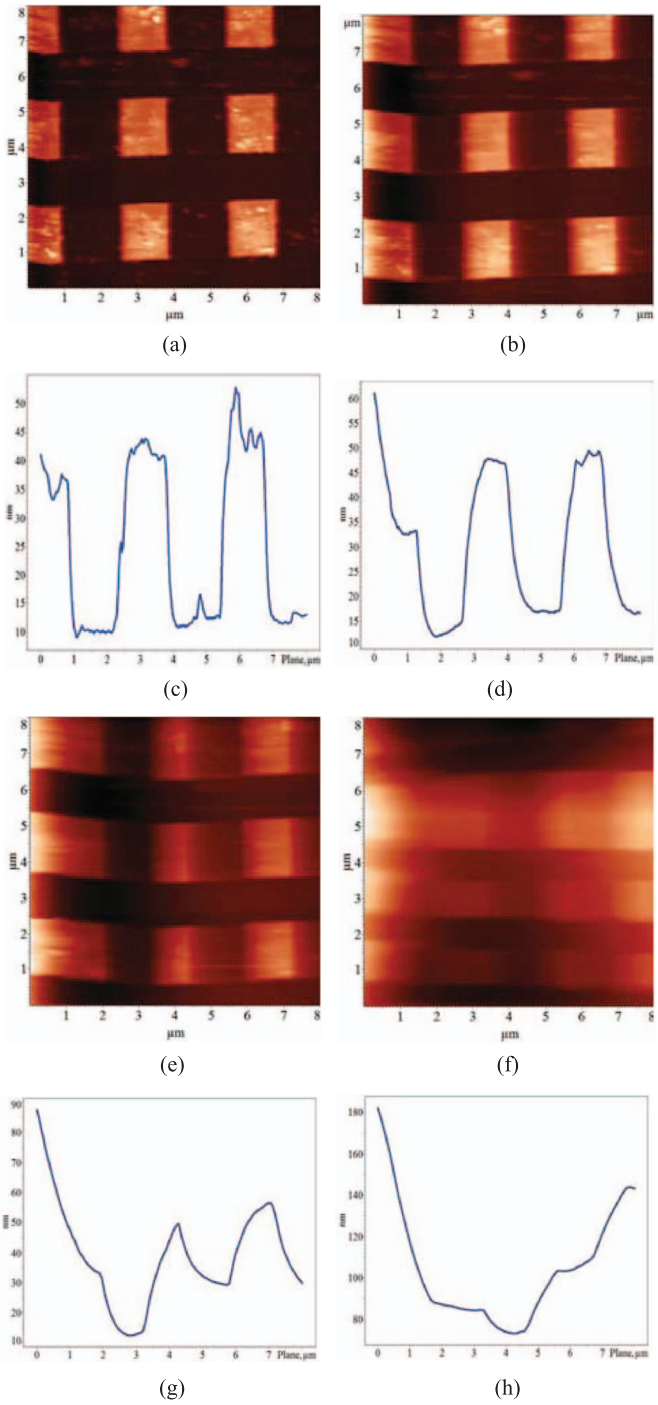

FIG. 9. Raster scanned images along with their intensity profiles. (a) 10.42 Hz PI image, (b) 62.5 Hz PI image, (c) 10 Hz, (d) 62.5 Hz, (e) 62.5 Hz PI image, (f) 125 Hz PI image, (g) 62.5 Hz, and (h)125 Hz.

line) signal achieves a good fit to the measured signal which improves imaging.

C. Image scanning performance

The proposed controller is implemented on the AFM for the spiral scanning of a TGQ1 standard calibration grating with a 20 nm surface height and 3 μm pitch (period). The instantaneous radius of the spiral is maintained at 6 μm and 512 lines, i.e., the diameter of the image contains 512 pixels. A constant-force AFM imaging mode is set up for spiral scanning and the Z deflection recorded to construct the spiral image, with the results observed by implementing the proposed controller in the X and Y-axes with the help of the dSPACE real-time system.

The generated spiral images scanned at 10, 30, 60, 120, 150, and 180 Hz frequencies along with their intensity profiles are shown in Figs. 8(a)–8(l). One point to note is that, the 2D planes of the images are not corrected for flatness, there are some uneven illuminations in them caused by imperfections, i.e., small inclination, dust, and additional physical properties. The inclination may be due to the tilted placement of the sample on the stage relative to the tip axis or improper surface finish of the sample.[43] The SPM images may be affected by hardware noise, miss-interaction of tip-sample during scanning, acoustic noises, and vibration effects of the scanner.[43] The scanned images using the proposed method have been filtered using a Gaussian filter to remove these effects from the image surface.

A set of raster scanned images using the AFM PI controller at 10.42, 31.25, 62.5, and 125 Hz (the reason for choosing these scanning frequencies is that they are the only ones above 10 Hz permitted by the AFM NT-MDT software), along with their intensity profiles, are presented in Figs. 9(a)–9(h) for comparison with the spiral scanned images. The spiral images are observed to be undistorted and follow the regular profile of the calibration grating. In contrast, the raster scanned images using the standard AFM PI controller become distorted and are affected by the induced vibration and high-speed dynamics of the PTS as the scanning frequency increases, as can be observed in Figs. 9(e) and 9(f). The spiral scanned images in Figs. 8(h) and 8(i) at 150 and 180 Hz frequencies have a circular wrapping effect but still better than the images using the in-built AFM PI controller in Figs. 9(e) and 9(f).

The surface intensity profile of the spiral scanned images is taken at y = 3 μm as shown in Figs. 8(d)–8(f) and 8(i)–8(l) at 10, 30, 60, 120, 150, and 180 Hz frequencies. Figures 9(c)–9(d) and 9(g)–9(h) show the intensity profile for the raster scanned images at y = 4 μm using the in-built AFM PI controller. This comparison demonstrates that the intensity profiles of the spiral scanned images are better captured than those of the raster scanned images using the in-built AFM PI controller.

VI. CONCLUSION

A high-speed spiral imaging method using an AFM is reported in this paper. In this work, an optimal LQG controller with vibration compensator is implemented on the AFM for faster and better-quality spiral image scanning. Experimental results show that, a significant improvement in the AFM imaging can be achieved by minimizing the adverse effects of scanner dynamics and it is demonstrated that a clearer and dimensionally more accurate image of a lattice structure of a sample can be obtained at higher scanning rates using the proposed scheme as compared to the traditional line-by-line (raster) scanning method. However, at higher scanning rates vibration becomes a barrier to the improvement.

ACKNOWLEDGMENTS

The authors would like to thank Mr. Shane Brandon for his help in the experiment. This work was supported by the Australian Research Council.

[1]G. Li, Y. Wang and L. Liu, IEEE Trans. Autom. Sci. Eng. **9**, 755 (2012).
[2]T. Junno, K. Deppert, L. Montelius, and L. Samuelson, Appl. Phys. Lett. **66**, 3627 (1995).
[3]D. M. Schaefer, R. Reifenberger, A. Patil, and R. P. Andres, Appl. Phys. Lett. **66**, 1012 (1995).
[4]M. Guthold, M. R. Falvo, W. G. Matthews, S. Paulson, S. Washburn, D. A. Erie, R. Superfine, F. P. Brooks, Jr., and R. M. Taylor, IEEE/ASME Trans. Mechatron. **5**, 189 (2000).
[5]M. Sitti and H. Hashimoto, IEEE/ASME Trans. Mechatron. **5**, 199 (2000).
[6]J. A. Main, E. Garcia, and D. V. Newton, J. Guid., Control, Dyn. **18**, 1068 (1995).
[7]M. Yves, *Scanning Probe Microscope* (SPIE, Bellingham, WA, 1995).
[8]G. Binnig, C. F. Quate, and C. Gerber, Phys. Rev. Lett. **56**, 930 (1986).
[9]I. A. Mahmood and S. O. R. Moheimani, Rev. Sci. Instrum. **80**, 063705(1) (2009).
[10]D. Zhiqiang, Z. Zude, A. Wu, and C. Youping, Int. J. Adv. Manuf. Technol. **32**, 1211 (2007).
[11]G. Schitter and M. J. Rost, Mater. Today **11**(Suppl.), 40 (2008).
[12]N. Tamer and M. Dahleh, in *Proceedings of the 33rd IEEE Conference on Decision and Control* (1994), p. 1826.
[13]H. Habibullah, H. R. Pota, I. R. Petersen, and M. S. Rana, IEEE Trans. Nanotechnol. **12**, 1125 (2013).
[14]H. Habibullah, H. R. Pota, I. R. Petersen, and M. S. Rana, IEEE/ASME Trans. Mechatron. **PP**, 1 (2013).
[15]K. Leang and S. Devasia, IEEE Trans. Control Syst. Technol. **15**, 927 (2007).
[16]B. Bhikkaji, M. Ratnam, A. Fleming, and S. O. R. Moheimani, IEEE Trans. Control Syst. Technol. **15**, 853 (2007).
[17]M. S. Rana, H. R. Pota, and I. R. Petersen, IEEE Trans. Nanotechnol. **12**, 246 (2013).
[18]A. Bazaei, Y. Yong, S. O. R. Moheimani, and A. Sebastian, IEEE Trans. Control Syst. Technol. **20**, 453 (2012).
[19]N. Chuang, I. R. Petersen, and H. R. Pota, in *Proceedings of the American Control Conference* (2011), p. 2258.
[20]S. Devasia, E. Eleftheriou, and S. O. R. Moheimani, IEEE Trans. Control Syst. Technol. **15**, 802 (2007).
[21]B. Bhikkaji and S. O. R. Moheimani, IEEE/ASME Trans. Mechatron. **13**, 530 (2008).
[22]J. Wang, J. Wang, Y. Hou, and Q. Lu, Rev. Sci. Instrum. **81**, 073705 (2010).
[23]I. A. Mahmood and S. O. R. Moheimani, Nanotechnology **20**(36), 365503 (2009).
[24]A. G. Kotsopoulos, A. Pantazi, A. Sebastian, and T. Antonakopoulos, in *Proceedings of the 18th IFAC World Congress,28 August –2 September* (2011), pp. 2018–2023.
[25]H. Habibullah, H. R. Pota, and I. R. Petersen, in *Proceedings of the 9th Asian Control Conference (ASCC)* (2013), pp. 1–6.
[26]H. Habibullah, I. R. Petersen, H. R. Pota, and M. S. Rana, in *8th IEEE Conference on Industrial Electronics and Applications (ICIEA)* (2013), pp. 1474–1479.
[27]I. A. Mahmood, S. O. R. Moheimani, and B. Bhikkaji, IEEE Trans. Nanotechnol. **10**, 203 (2011).
[28]P. Mansfield, J. Phys. C: Solid State Phys. **10**, L55 (1977).
[29]S.-K. Hung, J. Nanosci. Nanotechnol. **10**, 4511 (2010).
[30]W. Gao, J. Aoki, B.-F. Ju and S. Kiyono, Precis. Eng. **31**, 304 (2007).
[31]R. D. Hoge, R. K. S. Kwan, and G. Bruce Pike, Magn. Reson. Med. **38**(1), 117 (1997).
[32]Y. K. Yong, S. O. R. Moheimani, and I. R. Petersen, Nanotechnology **21**, 365503 (2010).
[33]A. G. Kotsopoulos and T. A. Antonakopoulos, Mechatronics **20**, 273 (2010).
[34]C. B. Ahn, J. H. Kim, and Z. H. Cho, IEEE Trans. Med. Imaging **5**, 2 (1986).
[35]See http://www.simplyphysics.com/page2_9.html for Free Induction decay signal.
[36]L. Ljung, Circuits, Syst. Signal Process. **21**(1), 11 (2002).
[37]P. Kabaila, IEEE Trans. Autom. Control **28**(1), 12 (1983).
[38]B. Friedland, *Control System Design, An Introduction to State Space Methods* (McGraw-Hill, New York, 1986).
[39]K. Chen, Y. Zhang, B. Lazzerini, and R. Yang, J. Electron. **27**(4), 557 (2010).
[40]A. E. Holman, P. M. L. O. Scholte, W. C. Heerens, and F. Tuinstra, Rev. Sci. Instrum. **66**(5), 3208 (1995).
[41]I. R. Petersen and A. Lanzon, IEEE Control Syst. Mag. **30**(5), 54 (2010).
[42]H. R. Pota, S. O. R. Moheimani, and M. Smith, Smart Mater. Struct. **11**(1), 1 (2002).
[43]V. L. Mironov, *Fundamentals of Atomic Force Microscopy* (The Russian Institute of Sciences, Institute for Physics and Microstructure, 2004).